

UC Berkeley

UC Berkeley Previously Published Works

Title

Manipulating chiral spin transport with ferroelectric polarization

Permalink

<https://escholarship.org/uc/item/62n598cg>

Journal

Nature Materials, 23(7)

ISSN

1476-1122

Authors

Huang, Xiaoxi

Chen, Xianzhe

Li, Yuhang

et al.

Publication Date

2024-07-01

DOI

10.1038/s41563-024-01854-8

Copyright Information

This work is made available under the terms of a Creative Commons Attribution-NonCommercial-NoDerivatives License, available at

<https://creativecommons.org/licenses/by-nc-nd/4.0/>

Peer reviewed



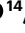

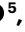





Manipulating chiral spin transport with ferroelectric polarization

Received: 19 June 2023

Accepted: 7 March 2024

Published online: 15 April 2024

 Check for updates

Xiaoxi Huang ^{1,18}, Xianzhe Chen ^{1,2,18} , Yuhang Li^{3,18}, John Mangeri^{4,18}, Hongrui Zhang ¹, Maya Ramesh⁵, Hossein Taghinejad⁶, Peter Meisenheimer ¹, Lucas Caretta¹, Sandhya Susarla ^{2,7}, Rakshit Jain ^{8,9}, Christoph Klewe ¹⁰, Tianye Wang ⁶, Rui Chen¹, Cheng-Hsiang Hsu ^{2,11}, Isaac Harris ⁶, Sajid Husain ^{1,2}, Hao Pan¹, Jia Yin¹², Padraic Shafer ¹⁰, Ziqiang Qiu ⁶, Davi R. Rodrigues ¹³, Olle Heinonen ¹⁴, Dilip Vasudevan ¹², Jorge Íñiguez ^{4,15}, Darrell G. Schlom ⁵, Sayeef Salahuddin^{2,11}, Lane W. Martin ^{1,2}, James G. Analytis ^{6,16}, Daniel C. Ralph ^{8,9}, Ran Cheng ^{3,17}, Zhi Yao ¹² & Ramamoorthy Ramesh ^{1,2,6} 

A magnon is a collective excitation of the spin structure in a magnetic insulator and can transmit spin angular momentum with negligible dissipation. This quantum of a spin wave has always been manipulated through magnetic dipoles (that is, by breaking time-reversal symmetry). Here we report the experimental observation of chiral spin transport in multiferroic BiFeO₃ and its control by reversing the ferroelectric polarization (that is, by breaking spatial inversion symmetry). The ferroelectrically controlled magnons show up to 18% modulation at room temperature. The spin torque that the magnons in BiFeO₃ carry can be used to efficiently switch the magnetization of adjacent magnets, with a spin-torque efficiency comparable to the spin Hall effect in heavy metals. Utilizing such controllable magnon generation and transmission in BiFeO₃, an all-oxide, energy-scalable logic is demonstrated composed of spin-orbit injection, detection and magnetoelectric control. Our observations open a new chapter of multiferroic magnons and pave another path towards low-dissipation nanoelectronics.

Intense studies of spin current transport in magnetic insulators^{1–7} have opened various avenues for research on spintronics^{7–13} and their potential use in low-power applications⁶. This trend has also triggered renewed interest in magnon physics, which can be controlled

via time-reversal-symmetry design (for example, magnetic domain walls¹⁴, spin Hall currents^{15,16} and static magnetic fields). On the other hand, recent works have shown that broken inversion symmetry and the resulting Dzyaloshinskii–Moriya interaction (DMI) have profound

¹Department of Materials Science and Engineering, University of California, Berkeley, CA, USA. ²Materials Sciences Division, Lawrence Berkeley National Laboratory, Berkeley, CA, USA. ³Department of Electrical and Computer Engineering, University of California, Riverside, CA, USA.

⁴Materials Research and Technology Department, Luxembourg Institute of Science and Technology, Esch/Alzette, Luxembourg. ⁵Department of Materials Science and Engineering, Cornell University, Ithaca, NY, USA. ⁶Department of Physics, University of California, Berkeley, CA, USA. ⁷School for Engineering of Matter, Transport and Energy, Arizona State University, Tempe, AZ, USA. ⁸Department of Physics, Cornell University, Ithaca, NY, USA. ⁹Kavli Institute at Cornell for Nanoscale Science, Ithaca, NY, USA. ¹⁰Advanced Light Source, Lawrence Berkeley National Laboratory, Berkeley, CA, USA. ¹¹Department of Electrical Engineering and Computer Sciences, University of California, Berkeley, CA, USA. ¹²Applied Mathematics and Computational Research Division, Lawrence Berkeley National Laboratory, Berkeley, CA, USA. ¹³Department of Electrical Engineering, Politecnico di Bari, Bari, Italy. ¹⁴Materials Science Division, Argonne National Laboratory, Lemont, IL, USA. ¹⁵Department of Physics and Materials Science, University of Luxembourg, Belvaux, Luxembourg. ¹⁶CIFAR Quantum Materials, CIFAR, Toronto, Ontario, Canada. ¹⁷Department of Physics and Astronomy, University of California, Riverside, CA, USA.

¹⁸These authors contributed equally: Xiaoxi Huang, Xianzhe Chen, Yuhang Li, John Mangeri. ✉ e-mail: xzchen@berkeley.edu; rramesh@berkeley.edu

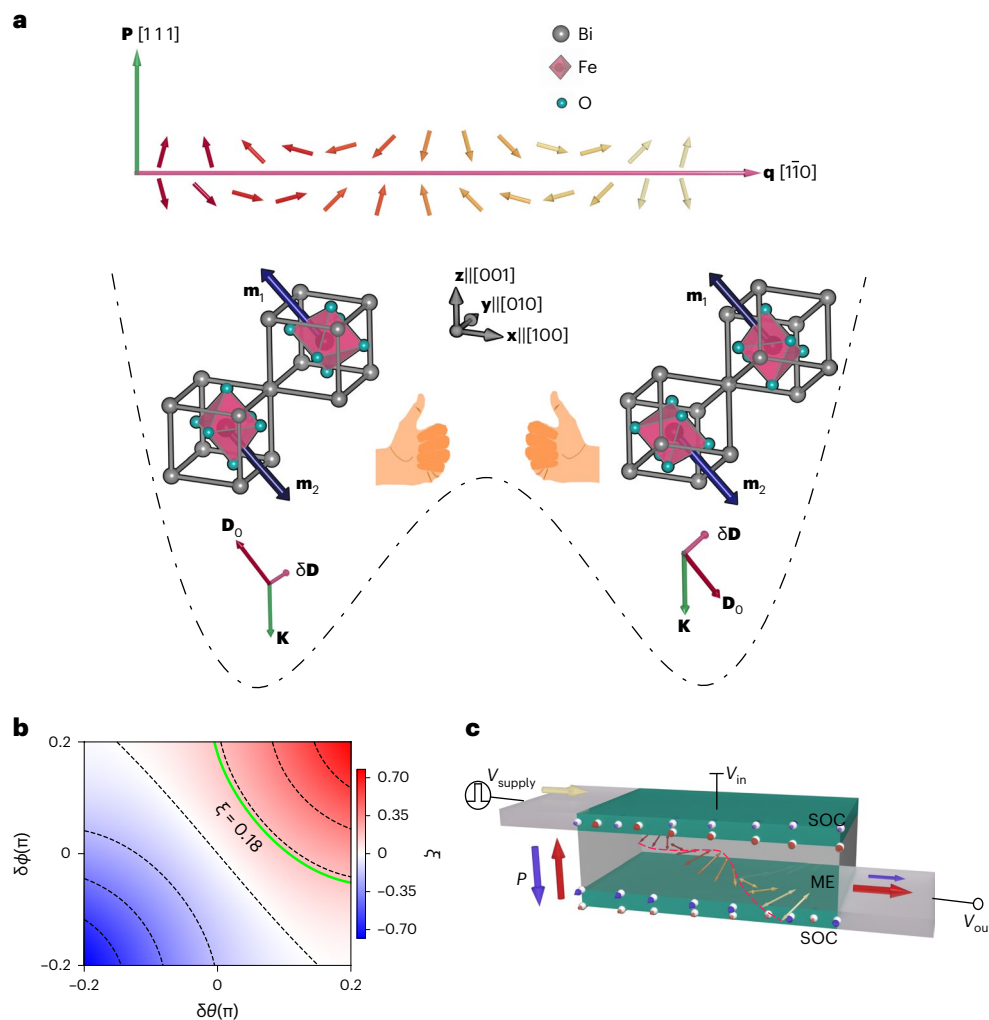


Fig. 1 | Concept of chiral magnon transport in multiferroics. **a**, A sketch of spin cycloid that propagates along $\mathbf{q} = [1\bar{1}0]$. \mathbf{P} is the ferroelectric polarization pointing along $[111]$, \mathbf{D}_0 (along $[\bar{1}\bar{1}2]$) is the intrinsic DMI vector responsible for the spin cycloid formation, and $\delta\mathbf{D}$ is the extrinsic DMI vector induced by the built-in electric field in BiFeO₃. The double well is a schematic of the bi-stable states of ferroelectric polarization. Upon the reversal of \mathbf{P} , \mathbf{D}_0 switches by 180° while $\delta\mathbf{D}$ remains unchanged, flipping the sign of the hybrid product $(\mathbf{D}_0 \times \delta\mathbf{D}) \cdot \mathbf{K}$, where \mathbf{K} is the magnon wave vector, hence causing a chirality flip of the three vectors. **b**, The modulation ratio of spin current (defined by equation (2)) as a function of $\delta\theta$ and $\delta\phi$, which are the spherical angles of $\delta\mathbf{D}$ ($\delta\mathbf{D} \approx 0.3\mathbf{D}_0$) relative to the

direction of \mathbf{D}_0 . The solid line marks the experimental value $\xi = 0.18$. The black dashed lines denote the ξ with equal value. **c**, The buffer logic consists of spin injection in the top SOC layer (dark green), magnetoelectric control of spin transmission in the intermediate magnetoelectric (ME) layer (translucent) and spin detection in the bottom SOC layer (dark green). The switching of the polar order is controlled by V_{in} . V_{supply} serves as the source for spin Hall current injection. The small (purple) and large (red) output voltages V_{out} in **c** correspond to spin transport of downward and upward ferroelectric polarization in **a**, respectively. The double-headed arrows denote the antiferromagnetic moments, and the red dashed line is used to describe how the antiferromagnetic moments rotate.

influence on magnon transport in non-centrosymmetric magnets^{17–19}. In this spirit, multiferroics are potentially of great interest, since they display broken inversion symmetry and a ferroelectric polarization that can be switched by the application of an electric field, which in turn allows for control of the magnetism and, potentially, the magnons. The idea that multiferroics could be promising candidates for magnonic manipulation has been considered for some time^{6,20}, but despite this early interest, observation and manipulation of magnon transport in multiferroics—that is, the capability to manipulate spin transport via ferroelectric polarization reversal and resultant DMI switching—remain elusive.

In this Article, we demonstrate non-volatile, bi-stable spin transport in multiferroic BiFeO₃ upon reversing the ferroelectric polarization. BiFeO₃ is a model multiferroic that exhibits multiple order parameters (that is, antiferromagnetism and ferroelectricity) and intrinsic magnetoelectric coupling of these co-existing order parameters^{21,22}. In the bulk, BiFeO₃ possesses a rhombohedrally distorted

perovskite structure in which a spin cycloid²³ is formed with a period length of ~62 nm (refs. 24,25) and a Néel temperature of ~643 K. The DMI in BiFeO₃ thin films can influence the spin cycloid order^{6,26,27}. At the same time, BiFeO₃ thin films possess robust ferroelectricity, with a Curie temperature ~1,100 K and a large polarization ~90 $\mu\text{C cm}^{-2}$ (ref. 28,29). In turn, BiFeO₃ exhibits outstanding magnetoelectric properties that have made it the focus of numerous studies hoping to utilize it as a platform to achieve low-energy (low-voltage) memory devices (for example, deterministic switching of adjacent ferromagnets³⁰). Specifically, achieving control over changing the magnetization states through ferroelectric polarization switching has always been a keen pursuit in these studies.

As illustrated in Fig. 1a, a spin cycloid propagating along $\mathbf{q} = [1\bar{1}0]$ is revealed by nitrogen vacancy (NV) diamond magnetometry measurements (Extended Data Fig. 1), which is in good agreement with the pioneering work of Gross et al.²⁴. The formation of spin cycloid has been explained in terms of a Lifshitz-like invariant that, in the

continuum limit, amounts to an effective DMI vector \mathbf{D}_0 (refs. 31,32), perpendicular to both the ferroelectric polarization \mathbf{P} (along [111]) and the spin cycloid propagating direction \mathbf{q} . In BiFeO₃, there is another intrinsic DMI characterized by a global DMI vector parallel to \mathbf{P} , which is responsible for the small magnetization \mathbf{m} everywhere perpendicular to the Néel vector \mathbf{L} . Due to the DMIs, the magnon band is circularly polarized (Extended Data Fig. 2). Previous studies have confirmed that the latter mechanism is relatively small so that the spin texture is dominated by \mathbf{D}_0 (refs. 31,32). A reversal of \mathbf{P} is accompanied by the reversal of the octahedral antiphase tilts³⁰ and the reversal of \mathbf{D}_0 (refs. 27,31). Specifically, for the vertical geometry (that is, Figs. 2 and 3), there will be the effects of asymmetries arising possibly from a built-in potential from the contacts in the heterostructure (that is, La_{0.7}Sr_{0.3}MnO₃/BiFeO₃/SrIrO₃ and SrRuO₃/BiFeO₃/SrIrO₃), which could induce an additional DMI vector $\delta\mathbf{D}$, which retains its direction when \mathbf{P} switches. Consequently, under such cases, the total DMI vector $\mathbf{D}_0 + \delta\mathbf{D}$ undergoes a non-180° switching, leading to a slight rotation of the propagation direction \mathbf{q} . Finally, a flexoelectric polarization induced by the strain gradient may also exist³³; however, its typical value is orders of magnitude smaller than the intrinsic ferroelectric polarization in BiFeO₃ and can thus be neglected. To intuitively understand the ferroelectric control of magnon spin current, we define the hybrid product $(\mathbf{D}_0 \times \delta\mathbf{D}) \cdot \mathbf{K}$, where \mathbf{K} is the magnon wave vector (in the thickness direction). It is well known that the non-reciprocal propagation is allowed not only in magnons but also in electromagnetic waves when they go through materials such as multiferroic materials that host broken time reversal and spatial inversion symmetry simultaneously. As illustrated in Fig. 1a, reversing \mathbf{P} necessarily flips \mathbf{D}_0 and hence the sign of $(\mathbf{D}_0 \times \delta\mathbf{D}) \cdot \mathbf{K}$ as well as the chirality of these three vectors. It is worth noting that this hybrid product can also reflect a directional non-reciprocity where the wave vector \mathbf{K} flips sign^{17,18,34} while the DMI is kept unchanged.

Because the thickness of BiFeO₃ is much smaller than the spatial period (~62 nm) of the spin cycloid, to first order, for simplicity we can ignore the effects of the spin texture or magnetic inhomogeneities along the magnon wave vector \mathbf{K} . Then, the transmitted spin current can be phenomenologically expressed as⁸

$$J_s = \frac{G_L}{S} \int d\mathbf{r}^2 [\mathbf{L}(\mathbf{r}) \cdot \mathbf{s}]^2 + \frac{G_m}{S} \int d\mathbf{r}^2 [\mathbf{m}(\mathbf{r}) \cdot \mathbf{s}]^2, \quad (1)$$

where G_L (G_m) is the phenomenological spin conductance of the Néel vector (total magnetization), $\mathbf{s} = \hat{y}$ is the polarization of spin injection from the top gate and S is the area of the film. As mentioned above, when the total DMI vector undergoes a non-180° switching, the spin cycloid profile functions $\mathbf{L}(\mathbf{r})$ and $\mathbf{m}(\mathbf{r})$ are modulated by \mathbf{P} in a non-trivial way. As calculated in Supplementary Information, the resulting spin current J_s can be substantially different before and after the reversal of \mathbf{P} . To quantify this difference, we define the modulation ratio as

$$\xi = \frac{J_s(-\mathbf{P}) - J_s(\mathbf{P})}{J_s(-\mathbf{P}) + J_s(\mathbf{P})} \quad (2)$$

and plot it against the orientation of the extrinsic $\delta\mathbf{D}$ relative to the intrinsic \mathbf{D}_0 (along $[\bar{1}\bar{1}2]$) in Fig. 1b, where we have marked the experimental value (to be explained below) $\xi = 0.18$.

Based on the predicted potential for chiral-magnon control in BiFeO₃, a demonstration of a scalable magnetoelectric spin-orbit logic was investigated. A schematic of this idea is illustrated in Fig. 1c. An electric field is set up in the magnetoelectric capacitor in the $-z$ direction, resulting in the vertical component of the ferroelectricity switching from the z to the $-z$ direction. To read the polarization state, a supply voltage is applied into the top spin-orbit coupled (SOC) channel (for example, SrIrO₃, which has a relatively large spin Hall angle³⁵)

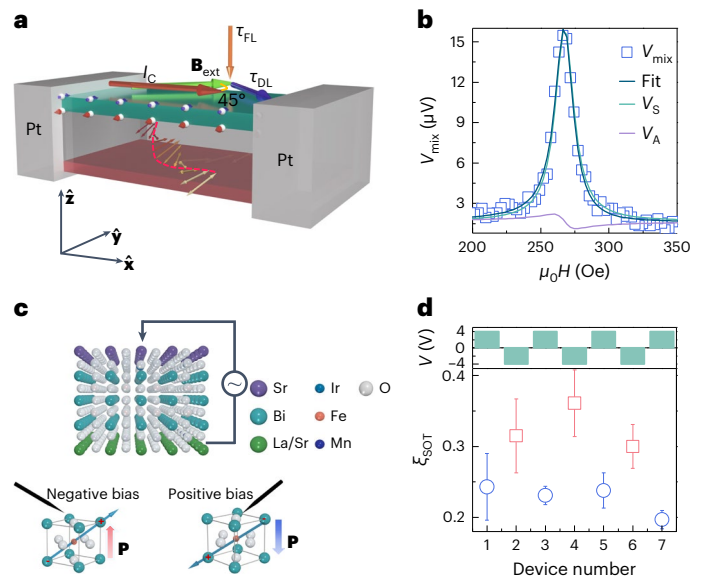


Fig. 2 | Spin transmission controlled by ferroelectric polarization in BiFeO₃.

a, A three-dimensional schematic illustration for the ST-FMR measurement: SrIrO₃ (top), BiFeO₃ (middle) and La_{0.7}Sr_{0.3}MnO₃ (bottom). I_c represents the radio frequency microwave current, which flows at a 45° angle with respect to the in-plane external magnetic field represented by \mathbf{B}_{ext} . A spin cycloid that lies in $(\bar{1}\bar{1}2)$ plane and propagates along $[\bar{1}\bar{1}0]$ direction is depicted by the double-headed arrows. **b**, The ST-FMR signal measured at room temperature for 12 dBm of applied microwave power at 4 GHz for a La_{0.7}Sr_{0.3}MnO₃ (20 nm)/BiFeO₃ (25 nm)/SrIrO₃ (10 nm) sample with dimensions of $5 \times 15 \mu\text{m}^2$. The lines are Lorentzian fits to the mixing voltage as described in Methods (‘ST-FMR analysis’ section), showing both symmetric and anti-symmetric components.

c, A schematic of a La_{0.7}Sr_{0.3}MnO₃ (20 nm)/BiFeO₃ (25 nm)/SrIrO₃ (10 nm) heterostructure subject to an external electric field, with schematics of the BiFeO₃ ferroelectric polarization under negative and positive biases. **d**, The SOT efficiency measured with the ST-FMR technique as a function of bias voltages applied beforehand for samples of La_{0.7}Sr_{0.3}MnO₃ (20 nm)/BiFeO₃ (25 nm)/SrIrO₃ (10 nm). The open squares (circles) represent the SOT efficiency for the tri-layer with negative (positive) bias voltages applied on the top electrode, SrIrO₃. The results represent the mean \pm standard deviation over SOT efficiencies at three frequencies ranging from 4.5 GHz to 5.5 GHz.

in the $+x$ direction, causing the excitation of magnons in the BiFeO₃ via the spin current from the SOC material³⁶. The readout of the state of the switch is then enabled by the inverse spin Hall effect (ISHE) using the bottom SrIrO₃ channel, where the current direction is along the x direction. Owing to the magnon propagation with bi-stable modulation, the output voltage could acquire two stable states, rendering the buffer function of a logic gate. Especially, as compared with the first magnetoelectric, spin-orbit (MESO) device proposal³⁷, this design makes use of antiferromagnetic magnon to gauge the antiferromagnetism inside the multiferroic itself instead of relying on the adjacent ferromagnet coupled to the multiferroic (Extended Data Fig. 3). Early efforts on the elimination of the ferromagnet have been devoted to the electric-field-controlled spin-orbit interaction³⁸, for example, the Rashba effect in two-dimensional electron gas systems³⁹. The elimination of the ferromagnet simplifies the readout architecture; furthermore, the implementation of antiferromagnets can favour ultrafast operations frequency up to THz.

To experimentally explore the controllable spin transmission enabled by the ferroelectric switch in BiFeO₃, we first characterized the strength of spin transmission via magnons in the heterostructures of the form La_{0.7}Sr_{0.3}MnO₃/BiFeO₃/SrIrO₃ (Methods, Extended Data Fig. 4 and Supplementary Fig. 1). We performed the measurement using a well-established technique, namely spin-torque ferromagnetic resonance (ST-FMR)^{35,40,41} (Fig. 2a), launching spin current using the

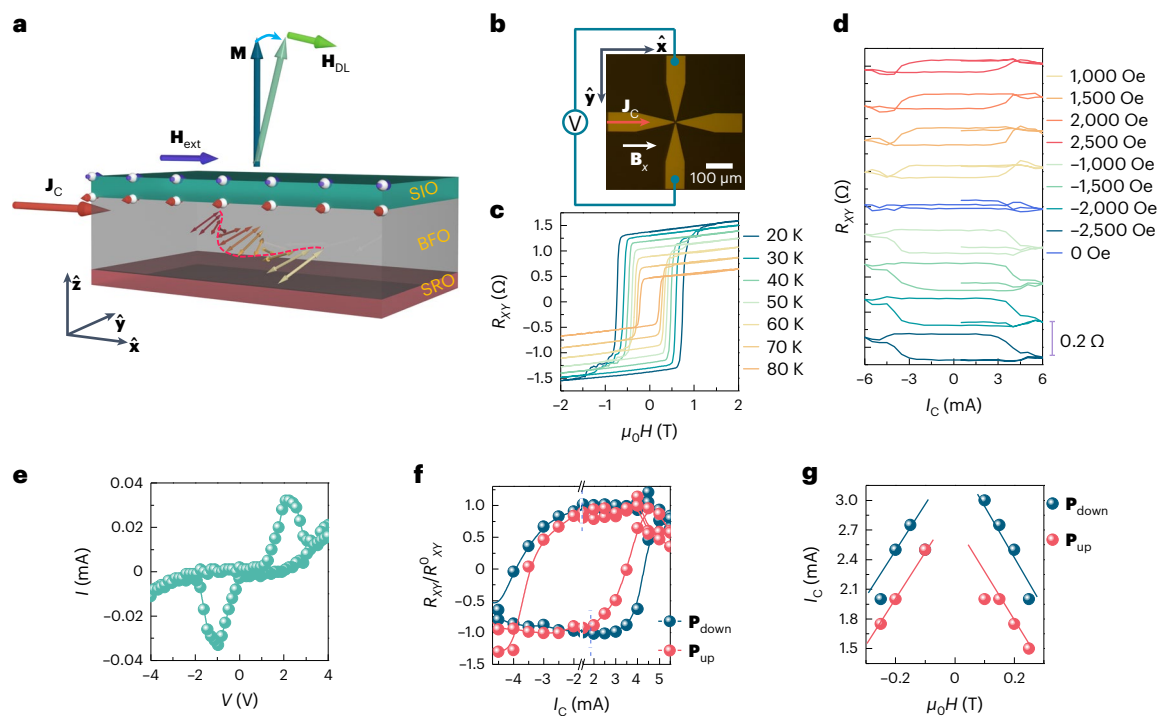


Fig. 3 | Magnetization switching induced by the spin-torque in BiFeO₃ under the control of ferroelectric polarization. **a**, A schematic demonstrating the magnetization switching of SrRuO₃ by the current-induced torques borne by the magnons transmitted through BiFeO₃ for a sample of SrRuO₃ (5 nm) (SRO)/BiFeO₃ (25 nm) (BFO)/SrIrO₃ (10 nm) (SIO). A spin cycloid that lies in the (11̄2) plane and propagates along the [11̄0] direction is depicted by the double-headed arrows. The torque carried by the transmitted magnons switches the magnetic moment (dark-green arrow) of the SrRuO₃ layer in the out-of-plane direction. **H_{ext}**, assisting magnetic field; **H_{DL}**, effective field due to damping-like torque; **M**, magnetization of SrRuO₃; **J_c**, injected electric current. **b**, An optical image of the Hall device used in the anomalous Hall effect (AHE) and magnetization switching measurements. **B_x**, magnetic field applied along the *x* direction. **c**, The anomalous Hall resistance (*R_{XY}*) as a function of the magnetic field at various temperatures for the heterostructure SrRuO₃ (5 nm)/BiFeO₃ (25 nm)/SrIrO₃ (10 nm) is shown on the bottom. A d.c. current of 100 μA is applied. **d**, *R_{XY}* as a function of pulsed currents at 70 K. External magnetic fields with different polarities and strengths are

applied along the current pulse direction to assist the magnetization switching. After each current pulse, a d.c. current of 100 μA is applied to detect the change in *R_{XY}*. The hysteretic magnetization switching loops are shifted with respect to the magnetization switching loop at zero assisting field for display. The current pulses have a pulse width of 1 ms. **e**, An example *I*-*V* curve collected during the ferroelectric switching experiments for the heterostructure SrRuO₃ (5 nm)/BiFeO₃ (25 nm)/SrIrO₃ (10 nm). **f**, An example ferroelectric polarization controlled magnetization switching measurement. The magnetization switching behaviour for a SrRuO₃ (5 nm)/BiFeO₃ (25 nm)/SrIrO₃ (10 nm) heterostructure with the polarization of BiFeO₃ pointing from the bottom (top) electrode to the top (bottom) electrode is shown in red (blue). The anomalous Hall resistance *R_{XY}* is normalized by *R_{XY}⁰* (anomalous Hall resistance at *I_c* = 0) for better display. **g**, The magnitudes of the critical switching current as a function of the assisting magnetic fields. The critical switching current for SrRuO₃ (5 nm)/BiFeO₃ (25 nm)/SrIrO₃ (10 nm) heterostructure with upward (downward) ferroelectric polarization is shown in red (blue). The lines are a guide to the eye.

large spin Hall effect of SrIrO₃ and detecting the spin torque applied to the magnetic La_{0.7}Sr_{0.3}MnO₃ layer⁴². An example ST-FMR spectrum, composed of both symmetric and anti-symmetric components, is shown in Fig. 2b and indicates the successful detection of the spin currents carried by magnons through BiFeO₃. To manipulate the orientation of the ferroelectric polarization, an external electric field was applied along the out-of-plane [001] direction to set the ferroelectric polarization of BiFeO₃ as illustrated (Fig. 2c, top, in which the top SrIrO₃ and the bottom La_{0.7}Sr_{0.3}MnO₃ layers serve as the two electrodes sandwiching the ferroelectric). Specifically, upward- (downward-) pointing polarization (180° switching) can be achieved by applying negative (positive) voltage larger than the coercivity of BiFeO₃ on the top SrIrO₃ layer (Fig. 2c, bottom)³⁹. After poling BiFeO₃ in each individual device to the desired polarization state, we then deposited platinum contacts onto the devices (contacting both the SrIrO₃ and La_{0.7}Sr_{0.3}MnO₃ layers) and performed ST-FMR measurements on the poled devices. By adopting an established analysis method (Methods), the spin-orbit torque (SOT) efficiency for the damping-like (DL) torque (symmetric component) is evaluated and summarized (Fig. 2d). We observe that the SOT efficiency can be set at a high value by negative (upward polarization) or at a low value by positive (downward polarization) voltages, indicating the presence of bi-stable high/low spin transport in BiFeO₃.

This polarization-dependent spin transmission of BiFeO₃ is also verified by interfacial engineering (Extended Data Fig. 5), time-resolved X-ray ferromagnetic resonance (Supplementary Fig. 2) and FMR measurements (Supplementary Figs. 3 and 4). The blocking temperature of exchange bias between La_{0.7}Sr_{0.3}MnO₃ and BiFeO₃ is well below room temperature⁴³, and the absence of exchange bias is also confirmed by our magneto-optic Kerr effect measurements (Supplementary Fig. 5), ruling out the possible contribution from exchange bias on the tuning of spin transmission. It is worthwhile to note that the stability of the ferroelectric polarization reveals another crucial advantage associated with spintronics produced in this manner: non-volatility. By setting the polarization direction, high and low SOT efficiencies of 0.33 and 0.23 can be achieved. Furthermore, the ferroelectric polarization controlled spin transmission in BiFeO₃ is confirmed by ST-FMR measurements on samples with opposite polarizations set by different interface terminations⁴⁴ (Extended Data Fig. 5). This is consistent with our theoretical predictions that the polarization state influences magnon propagation and a spin transmission modulation can be achieved upon switching the ferroelectric polarization. Further, from the aforementioned experiments, it can be inferred that the spin transmission is favourable when the magnon wave vector is anti-parallel to the *z* component of the polarization **P**.

To corroborate the presence of a magnon transmission modulation in BiFeO₃, magnetization switching experiments were carried out to serve as a direct demonstration of the strength of the spin torques under ferroelectric polarization modulation. Here, we investigate deterministic magnetization switching of a SrRuO₃ layer with perpendicular magnetic anisotropy (PMA) by the spin torque carried by BiFeO₃. Current-induced magnetization switching measurements were carried out for the SrRuO₃ (5 nm)/BiFeO₃ (25 nm)/SrIrO₃ (10 nm) heterostructure with BiFeO₃ polarized to either upward or downward orientation (Fig. 3a). The switching schematic is demonstrated in Fig. 3a. The magnetic switching was detected by the anomalous Hall effect in the SrRuO₃ layer, in which magnetic moments lying on the positive and negative directions can be distinguished by positive and negative values of anomalous Hall resistance. By sweeping an external magnetic field in the out-of-plane direction (Fig. 3b), a hysteretic loop is developed for anomalous Hall resistance (R_{xy}), when the external magnetic field exceeds the coercivity of SrRuO₃ (Fig. 3c). Furthermore, R_{xy} as a function of magnetic field was repeated at temperatures from 20 K to 80 K, confirming the high quality of our heterostructure, and no shift in the hysteretic loop with respect to zero magnetic field is observed, indicating the absence of exchange bias effect between ferromagnetic SrRuO₃ and antiferromagnetic BiFeO₃. Then magnetization switching measurements were performed in the same device at 70 K, and R_{xy} as a function of current pulses was recorded (Fig. 3d). Notably, a switching of magnetization was observed by both positive and negative currents, when the magnitudes of current pulses exceed the magnitude of critical switching current, and a saturation of R_{xy} is observed with large current pulses, excluding the possible participation of thermal effects in the switching measurements. Moreover, no magnetization switching is observed at zero assisting magnetic field and the switching chirality can be changed by the reversal of polarity of assisting magnetic fields, ruling out the possibility that the magnetization switching is caused by current-induced Oersted field. To further corroborate our observation of ferroelectric polarization-controlled spin transport with ST-FMR, ferroelectric polarization-dependent magnetization switching measurements were carried out. To start with, the polarization of BiFeO₃ was switched to either an upward or downward orientation by an external electric field, before the deposition of Pt electrodes that simultaneously contact both the top SrIrO₃ and bottom SrRuO₃ layers. An example I - V curve during the ferroelectric polarization switching measurements is displayed in Fig. 3e, in which the switching of ferroelectric polarization is associated with current peaks in Fig. 3e. Then, the same magnetization switching measurements were conducted on devices with distinct ferroelectric polarization states. A typical switching loop for heterostructures with upward (downward) polarization is displayed by red (blue) solid spheres in Fig. 3f. Strikingly, distinct critical switching currents for upward and downward polarization were observed in both positive and negative current directions. The critical switching currents at different assisting magnetic fields for upward and downward polarizations are summarized in Fig. 3g, where upward polarization shows a smaller switching current than downward polarization statistically. Therefore, two conclusions can be drawn on the basis of our experimental observations. First, BiFeO₃ has the capability to carry spin information via antiferromagnetic magnons⁴⁵, and the spin torque arising from BiFeO₃ is sufficient to switch the magnetization of SrRuO₃. More importantly, the spin transmission in BiFeO₃ is controlled by ferroelectric polarization, and the smaller critical switching current density for the upward polarization corresponds to a higher spin transmission, in good agreement with the ferroelectric polarization controlled-SOT efficiency study with the ST-FMR technique. The current-induced magnetization switching measurements reinforce the idea that the upward polarization is favourable for magnon transmission in vertical transport.

We further investigated the experimental demonstration of MESO via electrically controllable spin transport using a lateral non-local

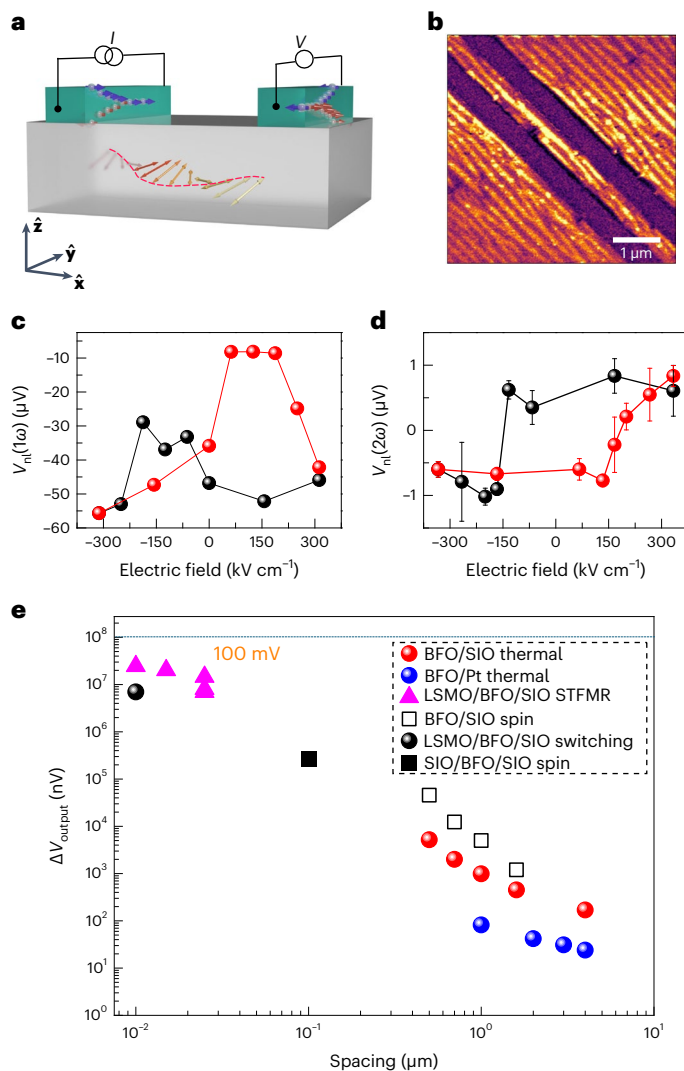


Fig. 4 | Magneto-electric spin-orbit logic based on controllable magnon transport in BiFeO₃. **a**, A schematic of the non-local device formed with a magneto-electric test structure. The purple and red arrows denote spins with opposite polarizations. The orange double-headed arrows represent the spin cycloid structure. **b**, A piezo-force microscopy image of the non-local device structure. The channel width is 0.5 μm . **c**, A hysteresis loop from the spin magnon readout in SrIrO₃ with first-harmonic measurements for a device with a 500 nm channel width. ω , frequency of the injected current. **d**, A hysteresis loop from the thermal magnon readout in SrIrO₃ with second-harmonic measurements in a device with a 1 μm channel width. Data are presented as mean \pm standard deviation of over 50 data points on a single device. **e**, Output voltage scaling with channel spacing for measurements in non-local devices (points for spacings 0.5 μm and above), vertical structure of SIO/BFO/SIO when BFO is 100 nm, and estimates of voltages that could be obtained for vertical transport of magnons through 10, 15 and 25 nm of BiFeO₃. The power is fixed at 3 mW. LSMO, La_{0.7}Sr_{0.3}MnO₃.

measurement. A schematic of the non-local measurement is provided in Fig. 4a; it consists of spin-orbit input and output via parallel source and detector wires, as well as magneto-electric control. Figure 4b illustrates well-ordered 71° ferroelectric domains, showing the high quality of the BiFeO₃ films. A non-local, quasi-static measurement was performed (Fig. 4c), varying the magnitude of the electric-field pulses applied in-the-plane across the channel from negative to positive and back again, and after each pulse measuring (over 100 s) non-local voltage signals due to magnon transport between the source and detector wires (Methods). We observe a hysteretic response in the magnon current launched by the spin Hall effect (first-harmonic

voltage; Fig. 4c) and the magnon current launched thermally by the local spin Seebeck effect (second-harmonic voltage; Fig. 4d), respectively, in which the coercive fields match each other. The first-harmonic hysteresis response also consists of an asymmetric shape. The overall details of the first-harmonic response appear to be dependent upon the measurement protocols (such as the current density used to carry out the spin Hall studies), and warrants more detailed studies. Besides, the electric field modulations of the output voltage can be obtained with d.c. methods, which can minimize the inductive and capacitive effect (Extended Data Figs. 6–8). Figure 4e shows measurements of the magnitude of these spin-transport signals as a function of channel spacing between the source and detector wires from 500 nm to 4 μm. The open squares reflect the magnitude of the signals associated with spin currents launched by the spin Hall effect (first-harmonic voltage), and the red circles reflect signals launched thermally by the spin Seebeck effect (second-harmonic voltage). Remarkably, the output voltage detected in BiFeO₃/SrIrO₃ stacks (~1 μV) is approximately one order of magnitude larger than the counterparts in BiFeO₃/Pt (~0.1 μV)⁴⁶, which is supported by the large spin–torque efficiency of SrIrO₃ previously observed with the ST-FMR measurement^{7,35} and the controlled non-local measurements of NiFe₂O₄/Pt and NiFe₂O₄/SrIrO₃ (Extended Data Figs. 9 and 10). The spacing dependence for both types of signal in BiFeO₃ fits well to the expectation for diffusive magnon propagation⁴⁷

$$R_{\text{nl}} = \frac{C}{\lambda} \frac{\exp(d/\lambda)}{1 - \exp(2d/\lambda)} \quad (3)$$

with effective diffusion lengths of ~0.17 μm (first harmonic) and ~0.25 μm (second harmonic).

Using this result and the spin–torque efficiencies obtained above (Fig. 2 and Extended Data Fig. 5), we can calculate the inverse-spin-Hall output voltage that would be obtained for a vertical geometry with BiFeO₃ thicknesses of 10, 15 and 25 nm using⁴⁸

$$V_{\text{ISHE}} = \frac{\theta_{\text{SOT}} \lambda_{\text{SD}} \tanh\left(\frac{t_{\text{SIO}}}{2\lambda_{\text{SD}}}\right) L}{t_{\text{SIO}} \sigma_{\text{SIO}}} J_s, \quad (4)$$

where we use the values of the spin–torque efficiency θ_{SOT} extracted from Fig. 2 and Extended Data Fig. 5, $\lambda_{\text{SD}} = 1.4$ nm (ref. 49) is the spin diffusion length of SrIrO₃, $t_{\text{SIO}} = 10$ nm is the thickness, $\sigma_{\text{SIO}} = 1 \times 10^5 \Omega^{-1} \text{m}^{-1}$ is the conductivity, $L = 10$ nm is the wire length and $J_s = 0.8 \times 10^9 \text{ A cm}^{-2}$. The output voltage is on the order of 10 mV, which is approaching the MESO target voltage of 100 mV. A prototypical magnon-mediated MESO logic device and its circuit modelling utilizing this ferroelectrically controlled magnon propagation are shown in Extended Data Fig. 3. So far, we have proven that the flow of spin information is viable in BiFeO₃ with the assistance of antiferromagnetic magnons and that the strength of the dissipationless magnon flow can be effectively manipulated by using external electric fields in a non-volatile fashion. This observation sheds light on implementing multiferroics as the potential spin carriers and opens new possibilities for energy-efficient magnonic spin logic devices.

Online content

Any methods, additional references, Nature Portfolio reporting summaries, source data, extended data, supplementary information, acknowledgements, peer review information; details of author contributions and competing interests; and statements of data and code availability are available at <https://doi.org/10.1038/s41563-024-01854-8>.

References

- Kruglyak, V. V., Demokritov, S. O. & Grundler, D. Magnonics. *J. Phys. D* **43**, 264001 (2010).
- Chumak, A. V., Vasyuchka, V. I., Serga, A. A. & Hillebrands, B. Magnon spintronics. *Nat. Phys.* **11**, 453–461 (2015).
- Kajiwara, Y. et al. Transmission of electrical signals by spin-wave interconversion in a magnetic insulator. *Nature* **464**, 262–266 (2010).
- Wang, H., Du, C., Hammel, P. C. & Yang, F. Antiferromagnonic spin transport from Y₃Fe₅O₁₂ into NiO. *Phys. Rev. Lett.* **113**, 097202 (2014).
- Chen, X. Z. et al. Antidamping-torque-induced switching in biaxial antiferromagnetic insulators. *Phys. Rev. Lett.* **120**, 207204 (2018).
- Wang, J. et al. Epitaxial BiFeO₃ multiferroic thin film heterostructures. *Science* **299**, 1719–1722 (2003).
- Zheng, D. et al. High-efficiency magnon-mediated magnetization switching in all-oxide heterostructures with perpendicular magnetic anisotropy. *Adv. Mater.* **34**, 2203038 (2022).
- Lebrun, R. et al. Tunable long-distance spin transport in a crystalline antiferromagnetic iron oxide. *Nature* **561**, 222–225 (2018).
- Chen, X. et al. Electric field control of Néel spin–orbit torque in an antiferromagnet. *Nat. Mater.* **18**, 931–935 (2019).
- Han, J. et al. Birefringence-like spin transport via linearly polarized antiferromagnetic magnons. *Nat. Nanotechnol.* **15**, 563–568 (2020).
- Chen, X. et al. Observation of the antiferromagnetic spin Hall effect. *Nat. Mater.* **20**, 800–804 (2021).
- Chen, X. et al. Octupole-driven magnetoresistance in an antiferromagnetic tunnel junction. *Nature* **613**, 490–495 (2023).
- Qin, P. et al. Room-temperature magnetoresistance in an all-antiferromagnetic tunnel junction. *Nature* **613**, 485–489 (2023).
- Han, J., Zhang, P., Hou, J. T., Siddiqui, S. A. & Liu, L. Mutual control of coherent spin waves and magnetic domain walls in a magnonic device. *Science* **366**, 1121–1125 (2019).
- Hamadeh, A. et al. Full control of the spin-wave damping in a magnetic insulator using spin–orbit torque. *Phys. Rev. Lett.* **113**, 197203 (2014).
- Zhou, Y. et al. Piezoelectric strain-controlled magnon spin current transport in an antiferromagnet. *Nano Lett.* **22**, 4646–4653 (2022).
- Moon, J.-H. et al. Spin-wave propagation in the presence of interfacial Dzyaloshinskii–Moriya interaction. *Phys. Rev. B* **88**, 184404 (2013).
- Gitgeatpong, G. et al. Nonreciprocal magnons and symmetry-breaking in the noncentrosymmetric antiferromagnet. *Phys. Rev. Lett.* **119**, 047201 (2017).
- Tokura, Y. & Nagaosa, N. Nonreciprocal responses from non-centrosymmetric quantum materials. *Nat. Commun.* **9**, 3740 (2018).
- Kimura, T. et al. Magnetic control of ferroelectric polarization. *Nature* **426**, 55–58 (2003).
- Chu, Y.-H. et al. Electric-field control of local ferromagnetism using a magnetoelectric multiferroic. *Nat. Mater.* **7**, 478–482 (2008).
- Zhao, T. et al. Electrical control of antiferromagnetic domains in multiferroic BiFeO₃ films at room temperature. *Nat. Mater.* **5**, 823–829 (2006).
- Rovillain, P. et al. Electric-field control of spin waves at room temperature in multiferroic BiFeO₃. *Nat. Mater.* **9**, 975–979 (2010).
- Gross, I. et al. Real-space imaging of non-collinear antiferromagnetic order with a single-spin magnetometer. *Nature* **549**, 252–256 (2017).
- Sando, D. et al. Crafting the magnonic and spintronic response of BiFeO₃ films by epitaxial strain. *Nat. Mater.* **12**, 641–646 (2013).
- Haykal, A. et al. Antiferromagnetic textures in BiFeO₃ controlled by strain and electric field. *Nat. Commun.* **11**, 1704 (2020).
- Ederer, C. & Spaldin, N. A. Weak ferromagnetism and magnetoelectric coupling in bismuth ferrite. *Phys. Rev. B* **71**, 060401(R) (2005).

28. Neaton, J. B., Ederer, C., Waghmare, U. V., Spaldin, N. A. & Rabe, K. M. First-principles study of spontaneous polarization in multiferroic BiFeO₃. *Phys. Rev. B* **71**, 014113 (2005).
29. Huang, Y.-L. et al. Manipulating magnetoelectric energy landscape in multiferroics. *Nat. Commun.* **11**, 2836 (2020).
30. Heron, J. et al. Deterministic switching of ferromagnetism at room temperature using an electric field. *Nature* **516**, 370–373 (2014).
31. Rahmedov, D., Wang, D., Íñiguez, J. & Bellaiche, L. Magnetic cycloid of BiFeO₃ from atomistic simulations. *Phys. Rev. Lett.* **109**, 037207 (2012).
32. Ramazanoglu, M. et al. Local weak ferromagnetism in single-crystalline ferroelectric BiFeO₃. *Phys. Rev. Lett.* **107**, 207206 (2011).
33. Zubko, P., Catalan, G. & Tagantsev, A. K. Flexoelectric effect in solids. *Annu. Rev. Mater. Res.* **43**, 387–421 (2013).
34. Wang, H. et al. Chiral spin-wave velocities induced by all-garnet interfacial Dzyaloshinskii–Moriya interaction in ultrathin yttrium iron garnet films. *Phys. Rev. Lett.* **124**, 027203 (2020).
35. Huang, X. et al. Novel spin–orbit torque generation at room temperature in an all-oxide epitaxial La_{0.7}Sr_{0.3}MnO₃/SrIrO₃ system. *Adv. Mater.* **33**, 2008269 (2021).
36. Mangeri, J. et al. Coupled magnetostructural continuum model for multiferroic BiFeO₃. *Phys. Rev. B* **108**, 094101 (2023).
37. Manipatruni, S. et al. Scalable energy-efficient magnetoelectric spin–orbit logic. *Nature* **565**, 35–42 (2019).
38. Noël, P. et al. Non-volatile electric control of spin–charge conversion in a SrTiO₃ Rashba system. *Nature* **580**, 483–486 (2020).
39. Lesne, E. et al. Highly efficient and tunable spin-to-charge conversion through Rashba coupling at oxide interfaces. *Nat. Mater.* **15**, 1261–1266 (2016).
40. Liu, L., Moriyama, T., Ralph, D. C. & Buhrman, R. A. Spin–torque ferromagnetic resonance induced by the spin Hall effect. *Phys. Rev. Lett.* **106**, 036601 (2011).
41. Liu, L. et al. Spin–torque switching with the giant spin Hall effect of tantalum. *Science* **336**, 555–558 (2012).
42. Merbouche, H. et al. Voltage-controlled reconfigurable magnonic crystal at the sub-micrometer scale. *ACS Nano* **15**, 9775–9781 (2021).
43. Yi, D. et al. Tailoring magnetoelectric coupling in BiFeO₃/La_{0.7}Sr_{0.3}MnO₃ heterostructure through the interface engineering. *Adv. Mater.* **31**, 1806335 (2019).
44. Yu, P. et al. Interface control of bulk ferroelectric polarization. *Proc. Natl Acad. Sci. USA* **109**, 9710–9715 (2012).
45. Cheng, R., Xiao, J., Niu, Q. & Brataas, A. Spin pumping and spin-transfer torques in antiferromagnets. *Phys. Rev. Lett.* **113**, 057601 (2014).
46. Parsonnet, E. et al. Non-volatile electric field control of thermal magnons in the absence of an applied magnetic field. *Phys. Rev. Lett.* **129**, 087601 (2022).
47. Cornelissen, L. J., Liu, J., Duine, R. A., Youssef, J. B. & Van Wees, B. J. Long-distance transport of magnon spin information in a magnetic insulator at room temperature. *Nat. Phys.* **11**, 1022–1026 (2015).
48. Shikoh, E. et al. Spin-pump-induced spin transport in p-type Si at room temperature. *Phys. Rev. Lett.* **110**, 127201 (2013).
49. Nan, T. et al. Anisotropic spin–orbit torque generation in epitaxial SrIrO₃ by symmetry design. *Proc. Natl Acad. Sci. USA* **116**, 16186–16191 (2019).

Publisher's note Springer Nature remains neutral with regard to jurisdictional claims in published maps and institutional affiliations.

Springer Nature or its licensor (e.g. a society or other partner) holds exclusive rights to this article under a publishing agreement with the author(s) or other rightsholder(s); author self-archiving of the accepted manuscript version of this article is solely governed by the terms of such publishing agreement and applicable law.

© The Author(s), under exclusive licence to Springer Nature Limited 2024

Methods

Sample growth

The tri-layers used in this study were grown by reflection high-energy electron diffraction (RHEED)-assisted pulsed laser deposition using a KrF laser with a wavelength of 248 nm. A 20 nm $\text{La}_{0.7}\text{Sr}_{0.3}\text{MnO}_3$ (5 nm SrRuO_3) layer was first grown at a substrate temperature of 700 °C and an oxygen partial pressure of 150 mTorr (100 mTorr), then a BiFeO_3 layer followed with various thicknesses at a substrate temperature of 700 °C and an oxygen partial pressure of 100 mTorr and finally a 10 nm SrIrO_3 layer finished the growth at a substrate temperature of 700 °C and an oxygen partial pressure of 50 mTorr. The films were grown at a repetition of 2(5) Hz, 10 Hz and 5 Hz with a laser fluence of 1.5 J cm^{-2} , 1.5 J cm^{-2} and 1.2 J cm^{-2} , respectively. After the growth, the sample was cooled to room temperature in an oxygen environment of 750 Torr at a cooling rate of 10 °C min^{-1} .

Ferroelectric polarization switching

The ferroelectric polarizations were switched using a ferroelectric tester (Precision Multiferroic, Radiant Technologies), with a fixed frequency of 10 kHz under room temperature. Two probes were placed on the SrIrO_3 (SIO) and ferromagnet (FM) layer, respectively, and two cycles of ferroelectric switching ($0 \rightarrow V_{\text{max}}$, $V_{\text{max}} \rightarrow -V_{\text{max}}$, $-V_{\text{max}} \rightarrow V_{\text{max}}$, $V_{\text{max}} \rightarrow -V_{\text{max}}$, $-V_{\text{max}} \rightarrow 0$) were carried out to make sure the ferroelectric polarization was fully switched. The final orientation of the ferroelectric polarization is determined by which electrode (top or bottom electrode) the drive voltage from the tester is positioned on.

Antiferromagnetic spin wave calculations

To perform the spin wave calculations shown in Supplementary Fig. 6, we first use the phase field method to prepare a polar ground state corresponding to $\mathbf{P}||[111]$ and $\mathbf{P}||[\bar{1}\bar{1}\bar{1}]$ (along with an order parameter for the octahedral antiphase tilts). We then evolve a damped sublattice Landau–Lifshitz–Bloch equation to find the magnetic ground states corresponding to $\mathbf{L}||[\bar{1}01]$, $\mathbf{m}||[\bar{1}\bar{2}1]$ and $\mathbf{L}||[10\bar{1}]$, $\mathbf{m}||[1\bar{2}1]$, respectively. The simulation approach is outlined in ref. 36. This homogeneous non-collinear magnetic ground state without a cycloid texture is then perturbed with an applied $\text{sinc}(x)$ field $\mathbf{H}||[\bar{1}01]$ with zero Gilbert damping ($\alpha = 0$), and the spin waves are set to propagate along $\pm \mathbf{k}||z$ in the linear limit. The detectable spin current in the AFM insulating layer⁴⁵ is proportional to $\mathbf{j} = \mathbf{j}^l + \mathbf{j}^m + \mathbf{j}^{ml} + \mathbf{j}^{lm}$ where $\mathbf{j}^l \propto \mathbf{l} \times \dot{\mathbf{l}}$, $\mathbf{j}^m \propto \mathbf{m} \times \dot{\mathbf{m}}$, $\mathbf{j}^{ml} \propto \mathbf{m} \times \dot{\mathbf{l}}$ and $\mathbf{j}^{lm} \propto \mathbf{l} \times \dot{\mathbf{m}}$. By time integrating the total spin current, the modulation (ratio) of *dc* components is found to be +0.978. Calculations are performed using the Ferret module, which is part of the open-source MOOSE framework⁵⁰.

ST-FMR analysis

The ST-FMR signal, V_{mix} , is produced across the $\text{La}_{0.7}\text{Sr}_{0.3}\text{MnO}_3/\text{BiFeO}_3/\text{SrIrO}_3$ ST-FMR device as a rectification of the anisotropic magnetoresistance that oscillates at the same frequency as the input microwave current I_{RF} (ref. 40). A microwave current at frequencies 4–6 GHz and power 12 dBm is applied to the device, with an in-plane external magnetic field oriented 45° with respect to the current direction. Finally,

$$V_{\text{mix}} = -\frac{1}{4} \frac{dR}{d\theta} \frac{\gamma_{\text{RF}} \cos\theta}{2\pi\Delta(df/dH)_{H_{\text{ext}}=H_0}} (\tau_{\text{DL}} F_S(\mathbf{H}_{\text{ext}}) + \tau_{\text{FL}} F_A(\mathbf{H}_{\text{ext}})) \quad (\text{ref. } 40),$$
 where $dR/d\theta$ is the angle-dependent magnetoresistance at θ , γ is the gyromagnetic ratio, Δ is the linewidth of the ST-FMR signal, $(df/dH)_{H_{\text{ext}}=H_0}$ is the field gradient of the resonance frequency, τ_{DL} is the DL torque, τ_{FL} is the field-like torque, $F_S(\mathbf{H}_{\text{ext}})$ is the symmetric Lorentzian function and $F_A(\mathbf{H}_{\text{ext}})$ is the anti-symmetric Lorentzian function, is detected by Keithley 2182A nanovoltmeter, from the fits of which the symmetric component V_S and the anti-symmetric component V_A , which are associated with DL torque (τ_{DL}) and field-like torque (τ_{FL}) respectively, can be extracted. As a result, the spin-orbit torque efficiency (ξ_{SOT}) is evaluated

using $\xi_{\text{DL}} = \frac{2e\tau_{\text{DL}} m_s t_{\text{FM}}}{j_c h}$, where $\tau_{\text{DL}} = \frac{4V_S \Delta}{r_{\text{RF}} \cos\theta} \frac{1 + \frac{\mu_0 M_{\text{eff}}}{2B_{\text{res}}}}{(1 + \frac{\mu_0 M_{\text{eff}}}{B_{\text{res}}})^{1/2}}$. The SOT efficiency

for the samples in this work was measured from 4 GHz to 6 GHz, and the error bar in Fig. 2 is a result of SOT efficiencies across different frequencies, while the error bar in Extended Data Fig. 5 is caused by the SOT efficiency distribution across different devices.

Device fabrication

To make ST-FMR devices, the samples were first spin coated with photoresist (MiR 701), and then devices with $50 \times 25 \mu\text{m}^2$ rectangular dimensions ($15 \times 10 \mu\text{m}^2$ for the electric-field-controlled experiment) were made by photolithography (Heidelberg MLA 150) followed by ion milling (Pi Scientific) that stopped at the $\text{La}_{0.7}\text{Sr}_{0.3}\text{MnO}_3$ layer. The remaining $\text{La}_{0.7}\text{Sr}_{0.3}\text{MnO}_3$ layer was used as the bottom electrode in the switching experiments; for the ST-FMR measurements, this was patterned using a H_3PO_4 wet etch (H_3PO_4 -to- H_2O ratio of 1:3). Finally, electrical contacts were made from 100 nm of Pt with a ground-signal-ground geometry, so that, when a ground-signal-ground high-frequency probe made contact with the samples, the current travelling through the Pt contacts did not produce a net Oersted field at the sample. Samples used in direct magnetization switching measurements consist of $\text{SrIrO}_3/\text{BiFeO}_3/\text{SrIrO}_3$. Hall crosses were patterned with a laser direct writer followed by ion milling and acid etching. SrRuO_3 was wet etched with an aqueous NaIO_4 (0.1 mol l^{-1}) solution. Electrical contacts of 100 nm Pt were made by a lift-off process. The non-local devices were defined using electron beam lithography and subsequent ion milling of the spin source layer on top. The separation between wires ranges from 4 μm to 500 nm.

Spin transport measurements

Transport measurements were conducted by employing four-terminal devices, wherein two terminals were dedicated to source current injection and the remaining two served as output terminals for ISHE voltage measurement. One source terminal and one detection terminal were also used to apply an electric field for ferroelectric polarization control. To measure the non-local ISHE voltage (V_{ISHE}), an SR830 lock-in amplifier was synchronized to both the first and second harmonic of the 7 Hz source current, isolating responses to the thermal gradients.

Spin texture imaging via NV microscopy

The imaging process was conducted at room temperature utilizing a Qnami ProteusQ scanning NV microscope. This microscope seamlessly integrates a confocal optical microscope with a tuning-fork-based atomic force microscope. Diamond tips featuring a parabolic taper and housing single NV centres, specifically the Quantilever MX+, were employed to enhance photon collection efficiency. The acquisition of large-area images for devices was carried out in the qualitative 'dual iso-B' mode. This mode leverages the NV centre's response to two distinct microwave frequencies to track the magnetic field. This approach greatly reduces data acquisition time compared with collecting the complete optically detected magnetic resonance spectrum.

Data availability

The data that support the findings of this study are available from the corresponding authors on reasonable request.

References

- Lindsay, A. D. et al. MOOSE: enabling massively parallel multiphysics simulation. *SoftwareX* **20**, 101202 (2022).

Acknowledgements

We are grateful for fruitful discussions with A. Fert, E. Parsonnet and Y. Huang. X.C., P.S., D.V., S.S., L.W.M., Z.Y. and R.R. acknowledge support from the U.S. Department of Energy, Office of Science, Office of Basic Energy Sciences, Materials Sciences and Engineering Division under Contract No. DE-AC02-05-CH11231 (Codesign of Ultra-Low-Voltage Beyond CMOS Microelectronics for the

development of materials for low-power microelectronics). X.H. and D.C.R. acknowledge support from the SRC-JUMP ASCENT centre. R.J. acknowledges support from the US Department of Energy, under contract no. DE-SC0017671. Y.L. and R.C. acknowledge support from the Air Force Office of Scientific Research under grant no. FA9550-19-1-0307. T.W. and Z.Q. acknowledge support from the US Department of Energy, Office of Science, Office of Basic Energy Sciences, Materials Sciences and Engineering Division under contract no. DE-AC02-05CH11231 (van der Waals heterostructures programme, KCWF16). This research used resources of the Advanced Light Source, which is a DOE Office of Science User Facility under contract no. DE-AC02-05CH11231. H.T. acknowledges support from the Bakar Fellows Program. H.P. acknowledges support from Army Research Office and Army Research Laboratory via the Collaborative for Hierarchical Agile and Responsive Materials (CHARM) under cooperative agreement W911NF-19-2-0119. J.M. has received funding from the European Union's Horizon 2020 research and innovation programme under the Marie Skłodowska-Curie grant agreement SCALES – 897614. D.R.R. acknowledges funding from the Ministero dell'Università e della Ricerca, Decreto Ministeriale n. 1062 del 10/08/2021 (PON Ricerca e Innovazione). O.H. acknowledges support from the US Department of Energy, Office of Science, Basic Energy Sciences, Division of Materials Sciences and Engineering.

Author contributions

X.C. and R.R. supervised this study. X.H. carried out the synthesis and characterization of heterostructures. X.H. and X.C. fabricated the devices. X.H. and R.J. carried out the ST-FMR measurements. X.H. and X.C. carried out the current-induced magnetization switching measurements. X.C. performed the non-local transport

measurements for BFO heterostructures. C.K. performed dynamic XMCD measurements at Beamline 4.0.2 of the Advanced Light Source. Y.L. and R.C. performed the theoretical calculations. J.M., D.R.R., O.H. and J.Í. developed and performed the coupled polar-micromagnetic simulations. X.C., Z.Y. and D.V. devised the electronic model and performed the calculations. S. Susarla performed the microstructure and electronic structure characterizations. H.Z., T.W., L.C., C.H.-H., I.H., S.H., H.P., J.Y., P.M., P.S., Z.Q., S. Salahuddin, M.R., D.G.S., L.W.M. and D.C.R. gave suggestions on the experiments. All authors discussed the results and prepared the manuscript.

Competing interests

The authors declare no competing interests.

Additional information

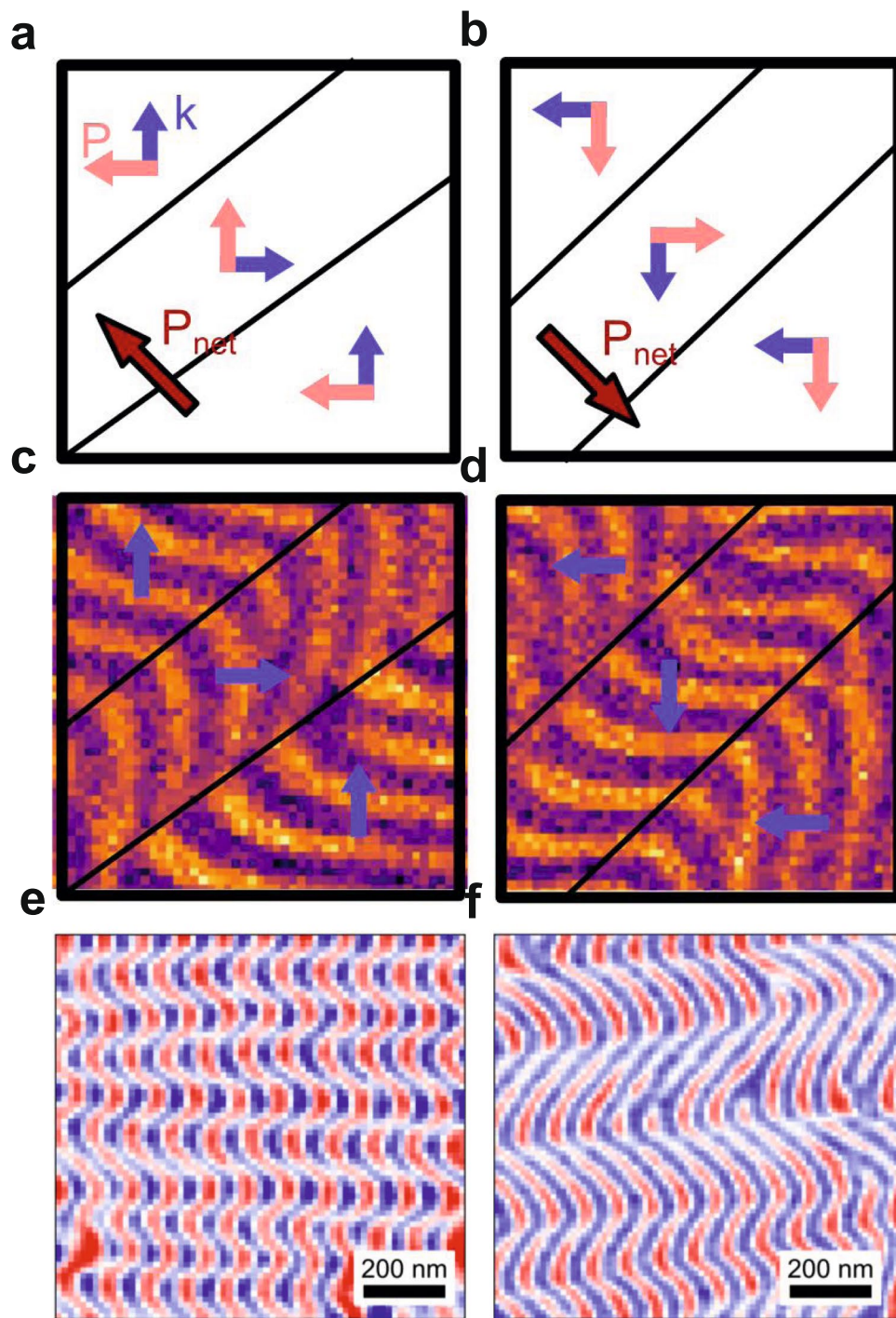
Extended data is available for this paper at <https://doi.org/10.1038/s41563-024-01854-8>.

Supplementary information The online version contains supplementary material available at <https://doi.org/10.1038/s41563-024-01854-8>.

Correspondence and requests for materials should be addressed to Xianzhe Chen or Ramamoorthy Ramesh.

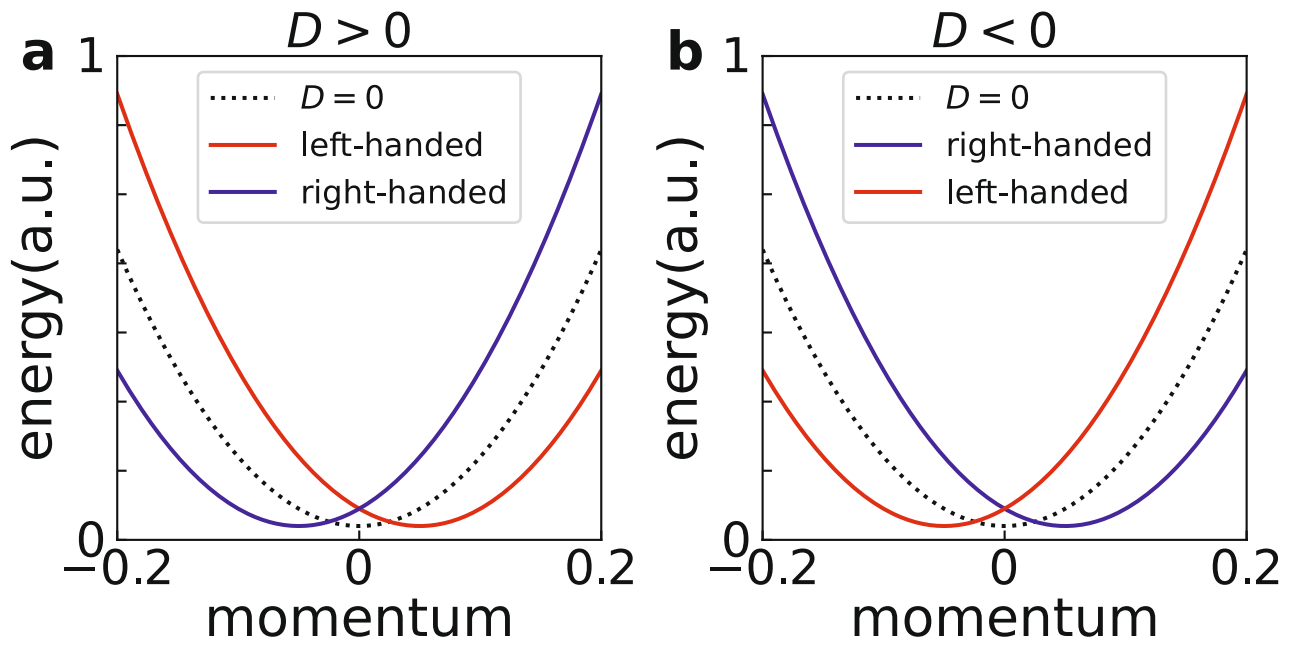
Peer review information *Nature Materials* thanks the anonymous reviewers for their contribution to the peer review of this work.

Reprints and permissions information is available at www.nature.com/reprints.



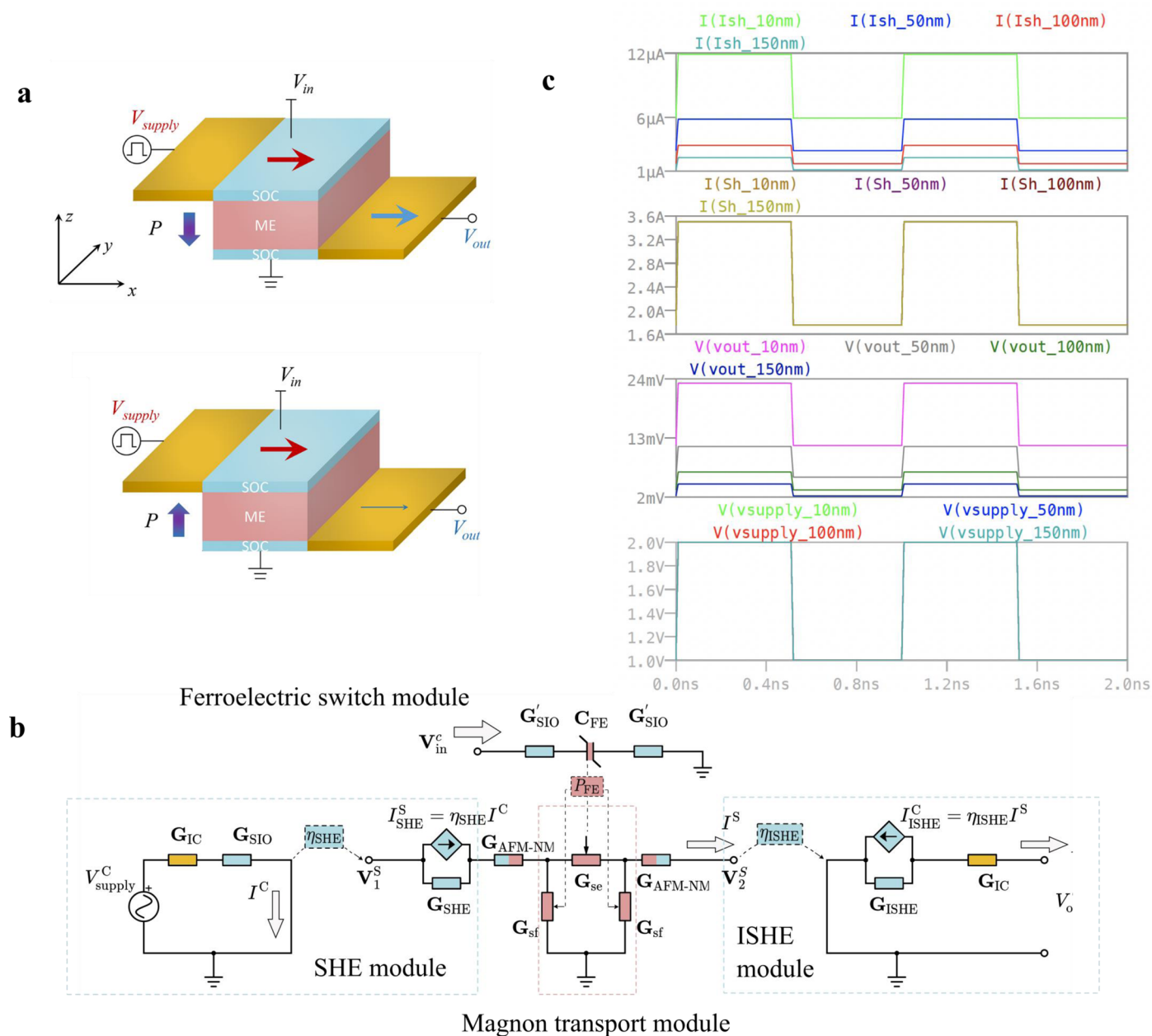
Extended Data Fig. 1 | NV magnetometry image for BiFeO₃. **a, b**, Schematic illustrations of ferroelectric domains and the corresponding spin cycloid propagation directions before and after polarization switching. The pink arrows represent the ferroelectric polarization orientations. **c, d**, Magnetic stray field

distribution recorded with scanning NV magnetometer for 100 nm BiFeO₃ before and after polarization switching. The blue arrows are the spin cycloid propagation wave vector. **e, f**, Magnetic stray field distribution recorded with scanning NV magnetometer for 30 nm and 100 nm BiFeO₃, respectively.



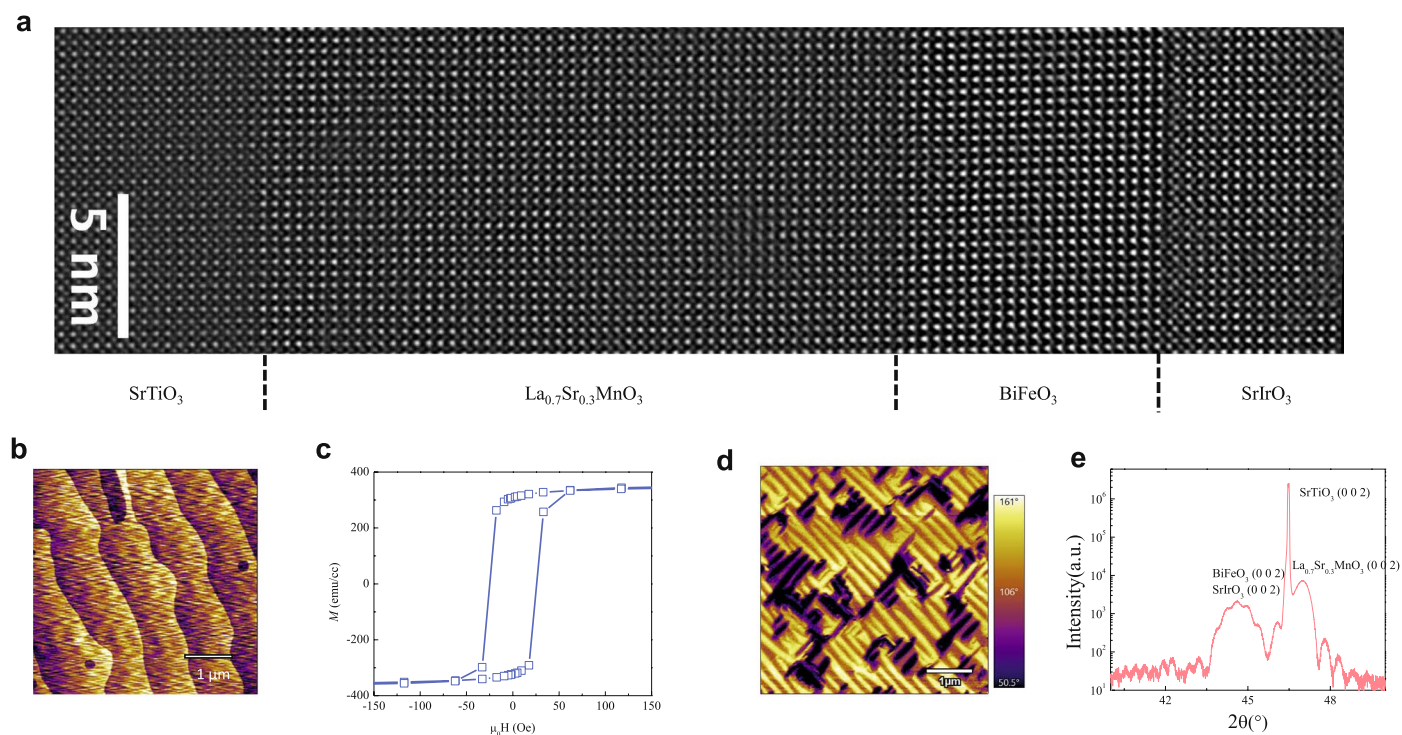
Extended Data Fig. 2 | Calculated magnon band for BiFeO₃. **a, b** magnon band dispersion for BiFeO₃ with negative and positive Dzyaloshinskii-Moriya interaction respectively. In the absence of the Dzyaloshinskii-Moriya interaction ($D=0$), magnon bands are doubly degenerate due to the combined PT-symmetry

(black dashed line). These degenerate magnon bands are linearly-polarized. Introducing Dzyaloshinskii-Moriya interaction breaks the degeneracy, resulting in two shifted circularly polarized magnon bands (lines in color).



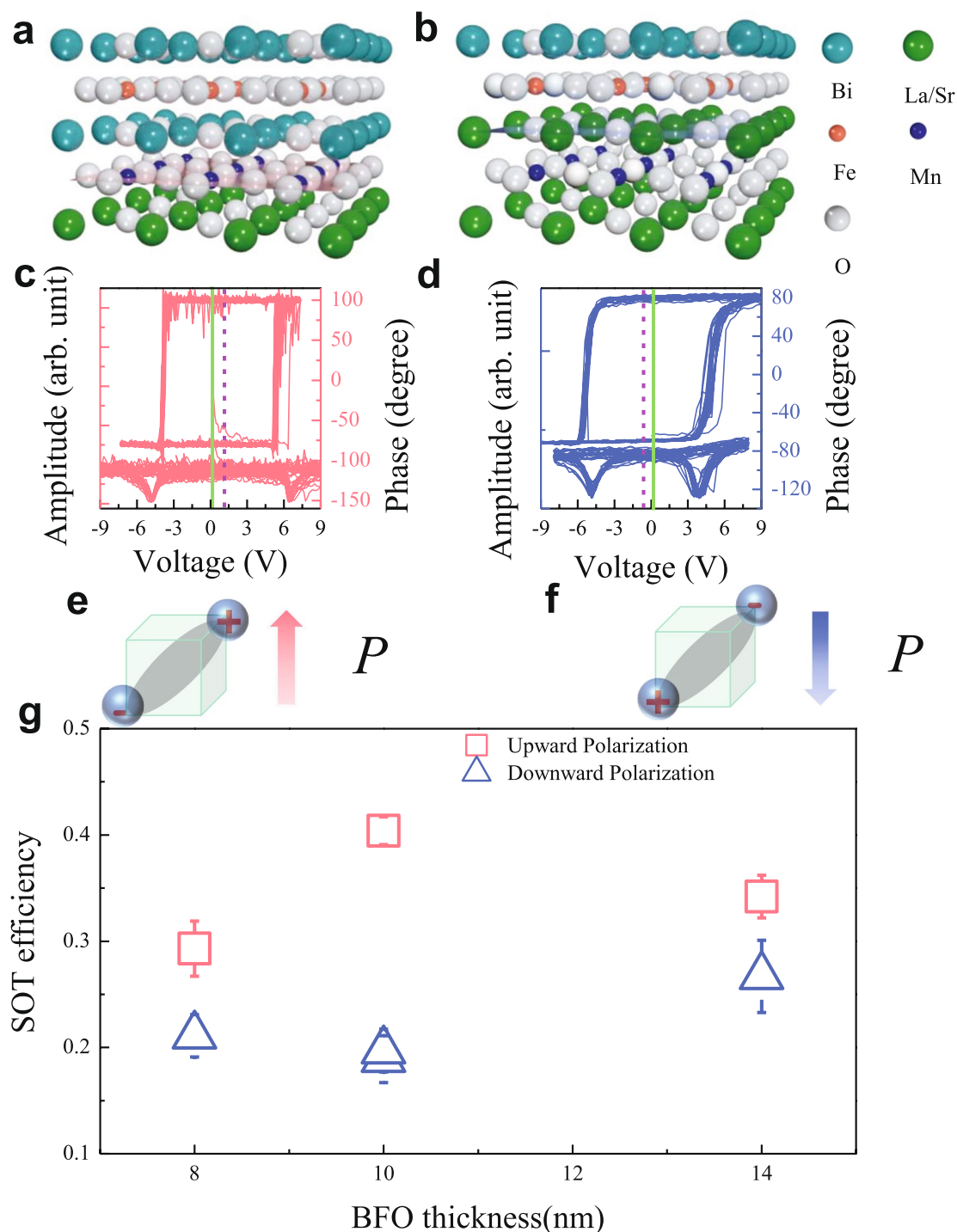
Extended Data Fig. 3 | Schematics for magnon-mediated MESO logic device.
a, Same schematics duplicated from Fig. 1c. **b**, Modularized circuit schematics. The top module is the ferroelectric switch module, where the input voltage V_{in}^c switches the direction of the ferroelectric polarization P_{FE} in the magnetoelectric layer. Such polarization change also affects the spin conductance G_{se} and G_{sf} of the ME layer. The leftmost and rightmost modules represent the spin Hall effect (SHE) process in the top SOC layer (injector) and the inverse spin Hall effect (ISHE) process in the bottom SOC layer (detector), respectively. The current-controlled spin current source I_{SHE}^c in the SHE module depends on the output

charge current of the top SOC layer. Similarly, the current-controlled charge current source I_{ISHE}^c in the ISHE module depends on the output spin current of the bottom SOC layer. The parameters η_{SHE} and η_{ISHE} represent the charge-to-spin and spin-to-charge current conversion rates, respectively. The module in the middle describes the magnon transport process in the ME layer, which is connected to the SHE and ISHE modules through the spin conductance at the interfaces between ME and SOC layers, denoted as G_{AFM-NM} . **c**, Lossy Buffer logic simulation result for the equivalent circuit in **b** where the output follows the input pulse signal characteristics.



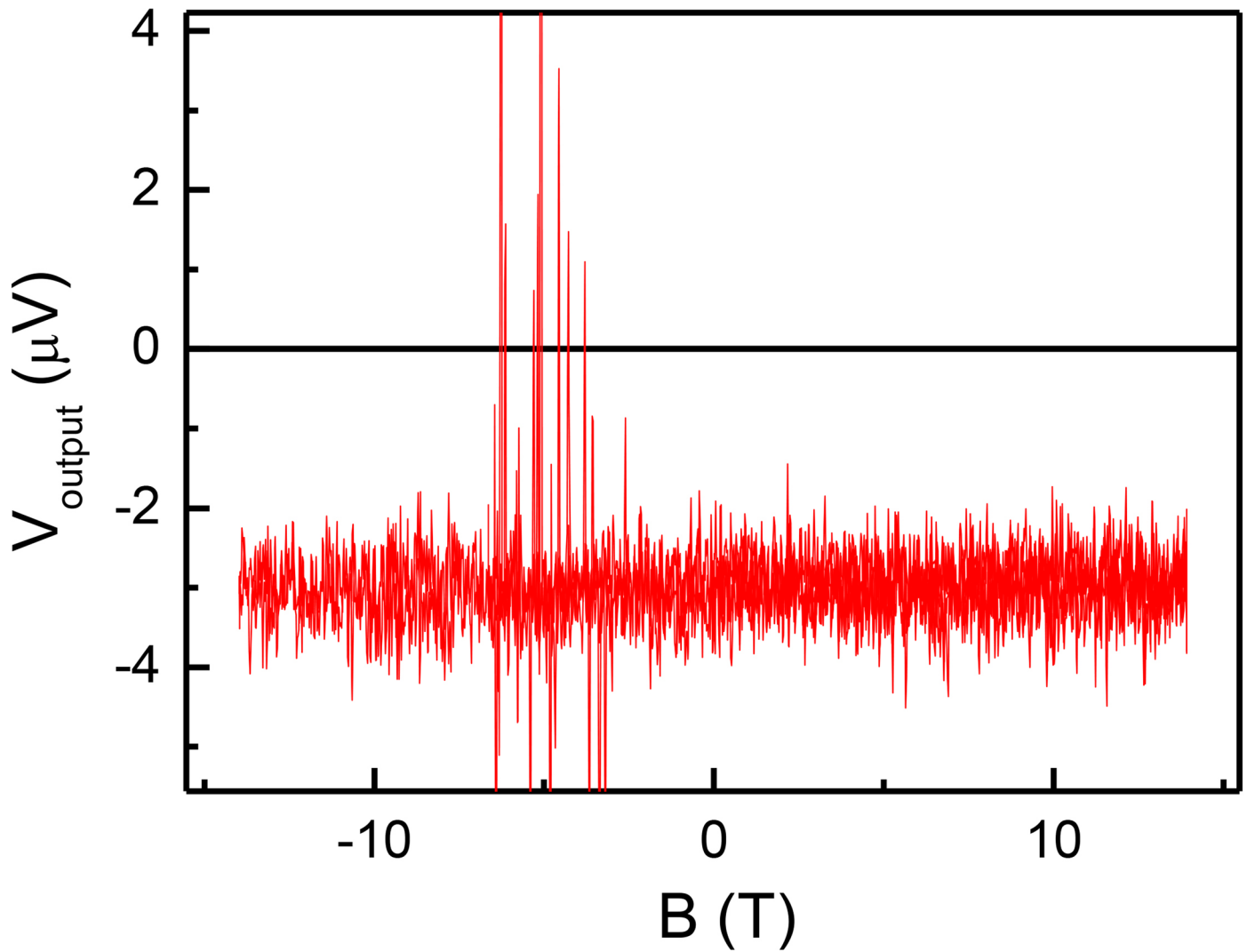
Extended Data Fig. 4 | Structure, magnetization, ferroelectric domain structure measurements for $\text{La}_{0.7}\text{Sr}_{0.3}\text{MnO}_3/\text{BiFeO}_3/\text{SrIrO}_3$ heterostructure. **a**, HAADF image of $\text{La}_{0.7}\text{Sr}_{0.3}\text{MnO}_3/\text{BiFeO}_3/\text{SrIrO}_3$ tri-layer, displaying atomically sharp interfaces and high crystal quality. **b**, HF etched and thermally annealed SrTiO_3 substrate with atomic steps and terraces. **c**, Magnetization vs applied

magnetic field (MH) measurement for $\text{La}_{0.7}\text{Sr}_{0.3}\text{MnO}_3/\text{BiFeO}_3/\text{SrIrO}_3$, showing a coercivity of ~ 25 Oe and a saturation magnetization ~ 320 emu/cc. **d**, In-plane piezoresponse microscopy (PFM) image of the BiFeO_3 layer. **e**, High resolution XRD 2θ - ω scan of the tri-layer.

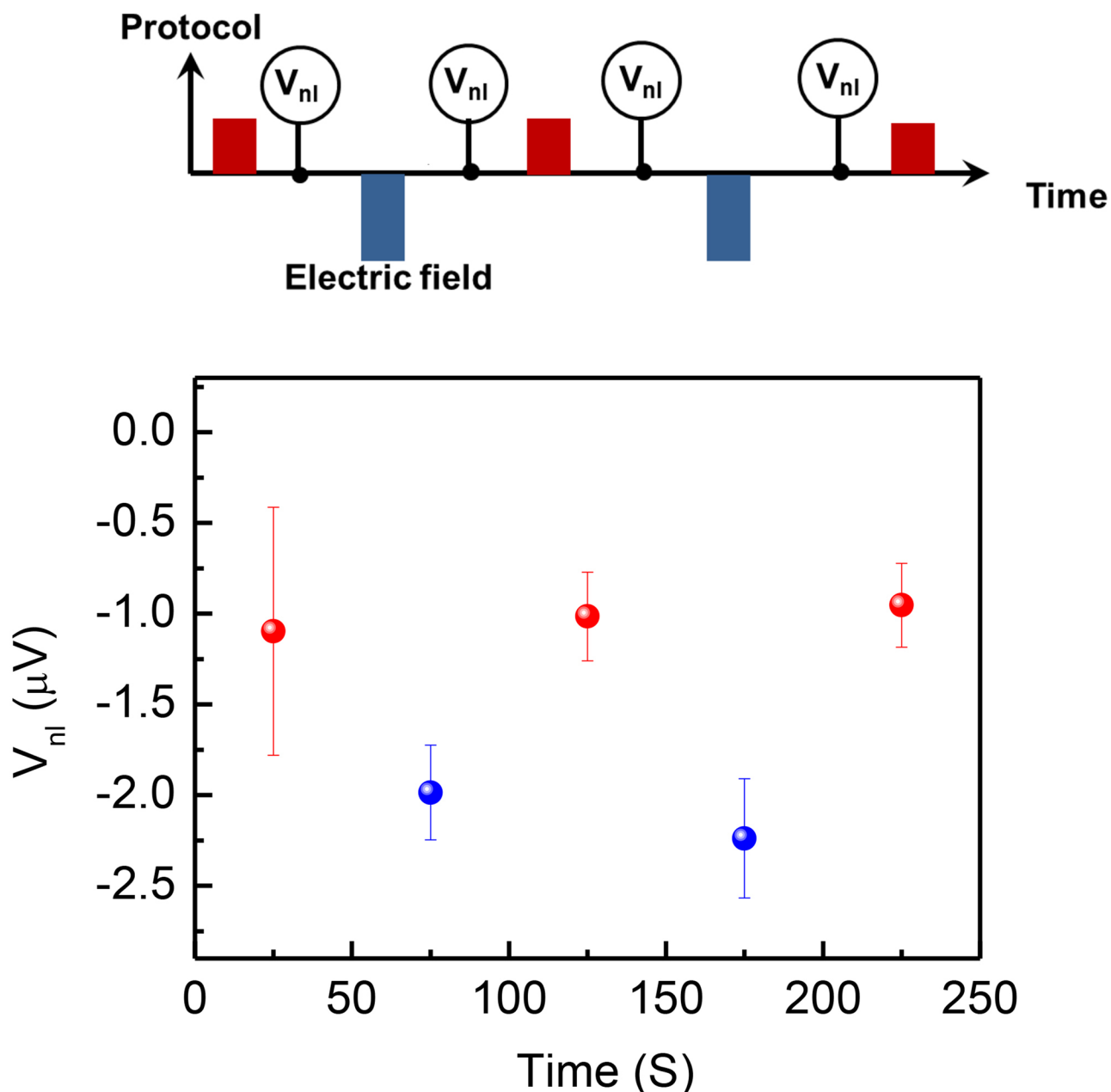


Extended Data Fig. 5 | Ferroelectric control of spin transport enabled by the interface chemistry. **a**, A schematic for $\text{La}_{0.7}\text{Sr}_{0.3}\text{MnO}_3/\text{BiFeO}_3$ atomic stacking, where $\text{La}_{0.7}\text{Sr}_{0.3}\text{O}-\text{MnO}_2-\text{BiO}-\text{FeO}_2$ is stacked at the interface. **b**, A schematic for $\text{La}_{0.7}\text{Sr}_{0.3}\text{MnO}_3/\text{BiFeO}_3$ atomic stacking, where $\text{MnO}_2-\text{La}_{0.7}\text{Sr}_{0.3}\text{O}-\text{FeO}_2-\text{BiO}$ is stacked at the interface. **c**, Corresponding piezoresponse for $\text{La}_{0.7}\text{Sr}_{0.3}\text{O}-\text{MnO}_2-\text{BiO}-\text{FeO}_2$ stacking ($\text{La}_{0.7}\text{Sr}_{0.3}\text{MnO}_3(12\text{ nm})/\text{BiFeO}_3(50\text{ nm})$), with top and bottom being phase and amplitude respectively. The solid line denotes the shifting of the piezoresponse curves to zero volts, indicating an upward ferroelectric polarization for $\text{La}_{0.7}\text{Sr}_{0.3}\text{O}-\text{MnO}_2-\text{BiO}-\text{FeO}_2$ stacking. **d**, Corresponding piezoresponse for $\text{MnO}_2-\text{La}_{0.7}\text{Sr}_{0.3}\text{O}-\text{FeO}_2-\text{BiO}$ stacking

($\text{La}_{0.7}\text{Sr}_{0.3}\text{MnO}_3(12\text{ nm})/\text{BiFeO}_3(50\text{ nm})$), with the top and bottom being phase and amplitude respectively. The solid line denotes the shifting of the piezoresponse curves to zero volts, indicating a downward ferroelectric polarization for $\text{MnO}_2-\text{La}_{0.7}\text{Sr}_{0.3}\text{O}-\text{FeO}_2-\text{BiO}$ stacking. **e, f**, An artistic illustration for upward and downward ferroelectric polarization. **g**, Spin orbit torque efficiency for BiFeO_3 with different polarization states as a function of BiFeO_3 thicknesses. The red (blue) data points represent the spin-orbit torque efficiency for $\text{La}_{0.7}\text{Sr}_{0.3}\text{MnO}_3/\text{BiFeO}_3/\text{SrIrO}_3$, where BiFeO_3 has an upward (downward) polarization. Data are presented as mean \pm standard deviation over 4 devices on a sample.

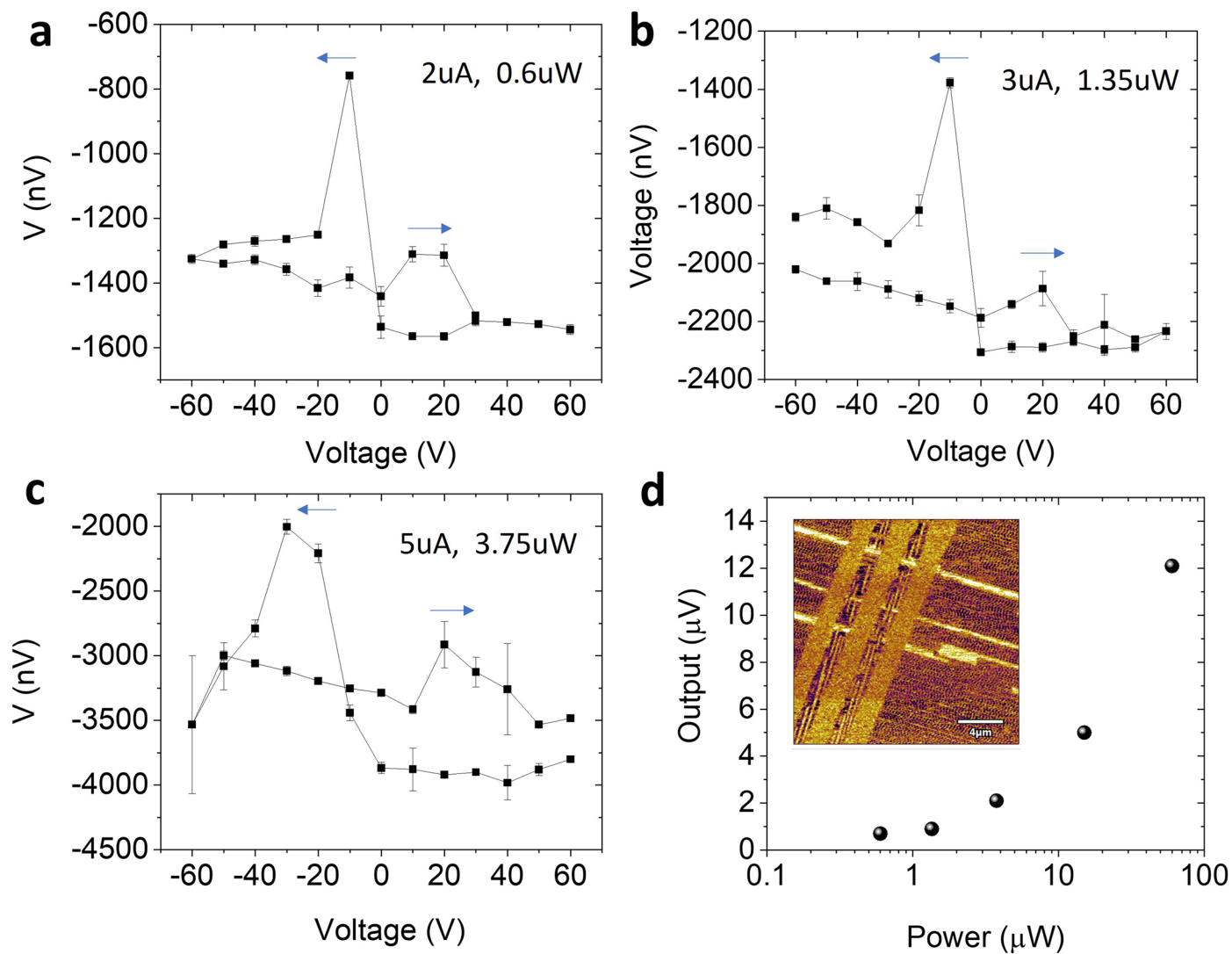


Extended Data Fig. 6 | Non-local voltage measured with sweeping external magnetic field. dc non-local voltage as a function of applied magnetic field at room temperature. The applied dc current is $10 \mu\text{A}$.

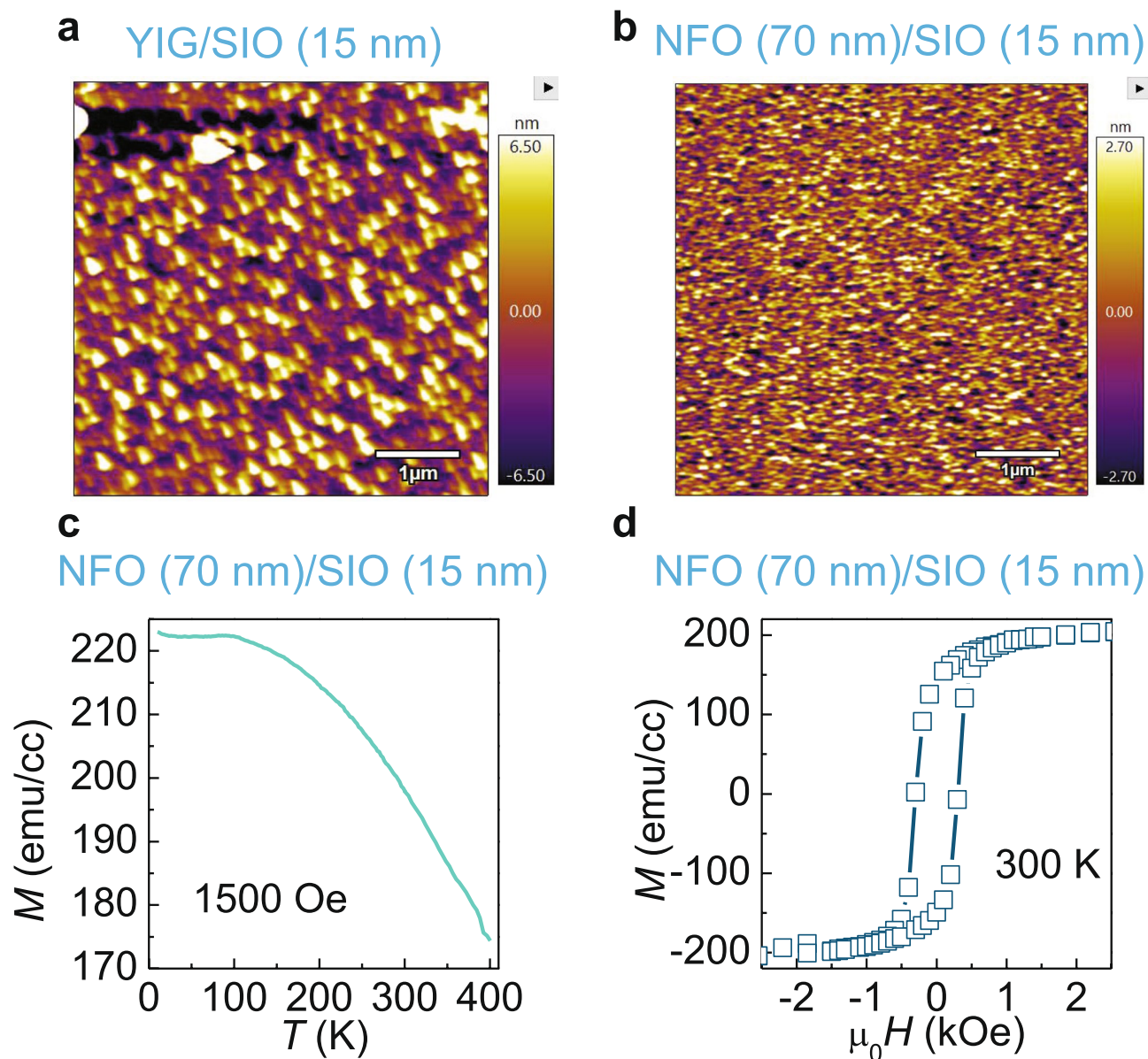


Extended Data Fig. 7 | Electric field controlled non-local spin transport measurements with dc current input. A positive electric field of 150 kV/cm and a negative electric field of -300 kV/cm are applied alternately, with dc non-local voltages measured in between the electric fields as shown in the measurement

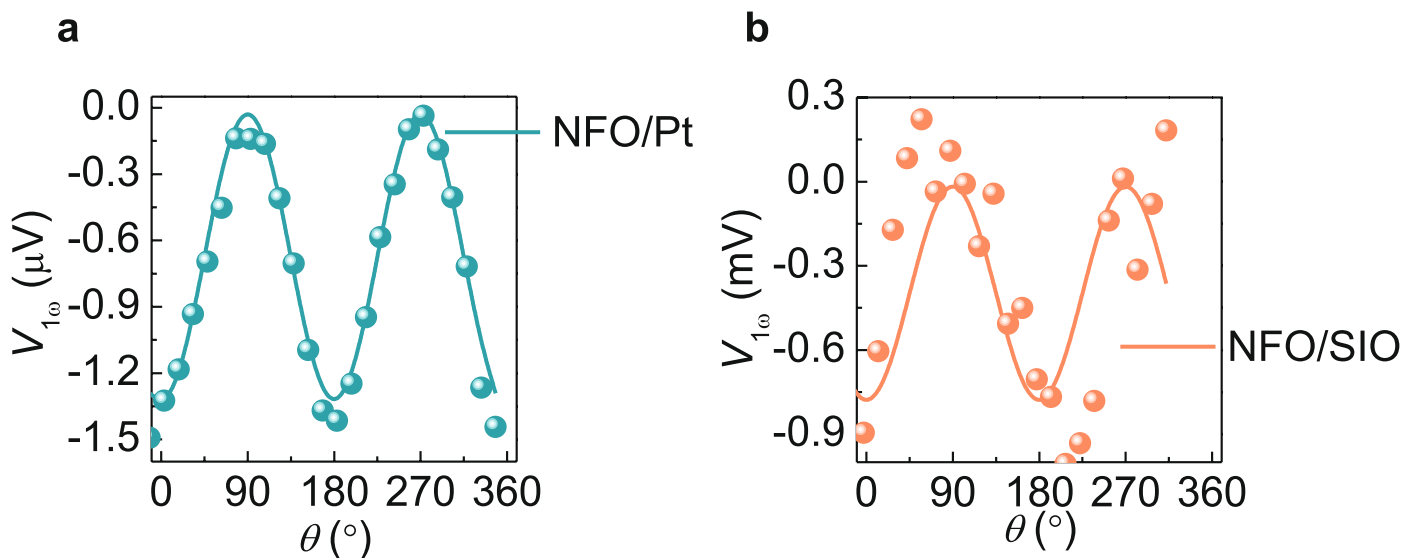
protocol. The corresponding non-local voltage between each electric field is shown below. Data are presented as mean \pm standard deviation of over 50 data points on a device.



Extended Data Fig. 8 | Power-dependent first-harmonic measurements in 71 degree domain BFO. a,b,c, Nonlocal out-put voltage with electric fields (voltage) scan when applying current of 2uA (a), 3uA (b), 5uA (c). **d,** Summary of power-dependent out-put voltages. Inset shows the PFM image. Data are presented as mean \pm standard deviation of over 50 data points on a device.



Extended Data Fig. 9 | AFM and SQUID characterization. **a**, An AFM image for SrIrO₃ (15 nm) grown on YIG/GGG structure. **b**, An AFM image for SrIrO₃ (15 nm) grown on NiFe₂O₄/STO structure. **c**, Magnetization as a function of temperature from 10 - 400 K, with a magnetic field of 1500 Oe applied in the plane. **d**, Magnetization as a function in-plane magnetic field at 300 K.



Extended Data Fig. 10 | Non-local control experiments on NiFe₂O₄ (70 nm)/Pt (5 nm) and NiFe₂O₄ (70 nm)/SrIrO₃ (15 nm). First harmonic voltage signal is displayed in **a** and **b** for NiFe₂O₄/Pt and NiFe₂O₄/SrIrO₃ respectively. An ac current with an amplitude of 100 μA and a frequency of 17 Hz was applied in a channel that is separated by 1 μm from the detection channel.